



# How to avoid false interpretations of Sentinel-1A TOPSAR interferometric data in landslide mapping? A case study: recent landslides in Transdanubia, Hungary

I. P. Kovács<sup>1</sup> · T. Bugya<sup>1</sup> · Sz. Czigány<sup>2</sup> · M. Defilippi<sup>3</sup> · D. Lóczy<sup>2</sup> · P. Riccardi<sup>3</sup> · L. Ronczyk<sup>1</sup> · P. Pasquali<sup>3</sup>

Received: 11 April 2018 / Accepted: 19 December 2018 / Published online: 29 December 2018  
© The Author(s) 2018

## Abstract

It is a crucial issue to better understand the usability of Sentinel-1 satellites in geomorphologic applications, since Sentinel-1 and the Copernicus Program are considered to be the workhorse of Earth observation by the European Space Agency during the next decades. Yet, a very limited experience is available on the applicability of Sentinel-1 images in the detection and identification of surface deformations and especially landslide mapping and monitoring in densely vegetated (low-coherence) areas. Few Synthetic Aperture Radar images (not more than 20) are sufficient for a successful run of interferometric stacking algorithms. This number is really low compared to the tremendous data flow of Sentinel-1 images that are available for interferometric analysis nowadays. Despite the availability of acquisitions, only a few papers exist on the accuracy of Sentinel-1 data, signal-to-noise ratio and the value of the acquired imagery for geomorphologic interpretation. Two test sites and a control site—affected by active surface deformations—have been investigated using 40 Sentinel-1A images and conventional persistent scatterers (PSI) method. PSI results have been combined with the geomorphologic information of the studied sites. We verified that the given number of Sentinel-1A acquisitions provide a unique base for surface deformation recognition and mapping in low-coherence areas. We found that scatterers were corrupted by a strong noise if their line of sight (LOS) velocity was below  $\pm 6\text{--}7$  mm/year all over the three test sites, although noise can easily be reduced. Noise reduction was achieved by a significant increase of the length of time series, i.e., time range between the first and last image to reduce the effect of atmospheric phase screen (APS).

**Keywords** Sentinel-1A · Persistent scatterer interferometry · High bluffs · Landslide · Atmospheric phase screen

---

✉ I. P. Kovács  
vonbock@gamma.ttk.pte.hu

<sup>1</sup> Department of Cartography and GIS, University of Pécs, Ifjúság útja 6, Pécs 7624, Hungary

<sup>2</sup> Department of Physical and Environmental Geography, University of Pécs, Ifjúság útja 6, Pécs 7624, Hungary

<sup>3</sup> sarmap SA, Cascio di Barico 10, 6989 Purasca, Switzerland

## 1 Introduction

Remotely sensed data such as orthophotographs, satellite images and LiDAR data are now essential materials for the analysis of surface deformation and, in particular, landslide mapping and monitoring (Chung and Fabbri 2003; Glade et al. 2005). Since Synthetic Aperture Radar (SAR) satellites were introduced in the early 1990s by launching ERS and Envisat, they have produced one of the most precise raw materials for the recognition of surface displacement. Processed C-band acquisitions have been found suitable for the detection of slow or extremely slow-moving landslides (Wasowski and Bovenga 2015).

Conventional processing technologies of SAR data, such as interferometric SAR processing (InSAR), operate with coherence calculated from SAR acquisition pairs (Béjar-Pizarro et al. 2017). Nonetheless, this technique has several limitations, which may affect the usability of InSAR deformation measurements (Casagli et al. 2016). Temporal and geometric decorrelation and mostly atmospheric artifacts reduce the spatial and temporal coherence and strongly affect displacement recognition (Hein 2004). Advanced differential interferometry (DInSAR) stacking techniques, such as persistent scatterers (PSI) (Ferretti et al. 2001; Tofani et al. 2013; Piacentini et al. 2015), overcome the limitation of InSAR (Pasquali et al. 2014) and make it suitable for landslide monitoring. Due to the popularity of ERS and Envisat acquisitions in landslide research, abundant information is available on their applicability and limitations (Herrera et al. 2010, 2013; Chen et al. 2014; Singleton et al. 2014; Tomás et al. 2014).

The Copernicus Programme of the European Space Agency has opened a new age in terms of SAR imagery. Sentinel-1 mission provides C-band regular imaging over wide areas of the globe. Due to the enhanced revisit frequency (12 days) and the short baseline, Sentinel-1 mission accelerates the application of InSAR technology over many countries (ESA 2013). Routine implementation of Sentinel-1 based InSAR application is just under development, but during the next 7 years (lifetime of Sentinel-1), there will be a significant progress in InSAR technology (ESA 2013).

Nonetheless, a very limited experience is available on the suitability of Sentinel-1 for the detection and identification of surface deformations (Sowter et al. 2016) and specifically for landslide mapping and monitoring (Barra et al. 2016). Sentinel-1A started its operational life in October 2014. More than 40 images, theoretically a sufficient number, were freely accessible and available for PSI analysis from the Copernicus Data Hub in the spring of 2016. However, the temporal distribution of Sentinel-1A images is fundamentally different from that of the routinely used ERS and Envisat. Forty images of Sentinel-1A cover only a period of approximately a year and a half (ca. 12 days repeat cycle), while the temporal coverage of the older C-band sensors spans for several years with the same number of images (ca. 35 days repeat cycle). Atmospheric phase screen (APS) filtering has been tuned for these satellites; thus, there is no information on the effectiveness of filtering techniques for the given number of Sentinel-1A images. The small orbital tube of the Sentinel-1 mission and inaccuracies in the reference digital elevation model (DEM), used during the processing, have also an impact on final data precision of interferometric deformation data. Moreover, there is a lack of knowledge on how the new advanced sensor signal-to-noise ratio affects the recognition of active landslides (Casagli et al. 2016). Since Sentinel satellites are thought to be the workhorse of Earth Observation (EO) projects, it is crucial to understand their applicability in landslide research (Prats-Iraola et al. 2015).

Therefore, the aim was to test the strengths and limitations of Sentinel-1A acquisitions in surface deformation recognition, using PSI interferometric technique. The main questions to answer were the following:

- (1) Does the processing of data collected over a short period of time (less than 2 years) by the Sentinel-1A sensor provide adequate and accurate information on the spatial separation of stable background and active landslides?
- (2) Is it possible to differentiate between sensor noise and real signals of surface deformation?

The paper is intended for scientists and end-users involved in data interpretation for surface deformation associated with mass movements.

## 1.1 Geomorphologic settings

To answer the above questions, two test sites and a control site—affected by active surface deformations—were chosen for PSI analysis. Surface deformations, including landslides, are common in mountainous and hilly regions and along the Danube River in Hungary (Szabó 1996). Due to the lateral erosion of the Danube, a 20–60 m high bluff series of Late Miocene (Pannonian) lacustrine clays and silts, Pliocene terrestrial red and reddish clays and Pleistocene loess and paleosol sequences has been formed on the right bank of the river (Pécsi 1959). The most likely preconditioning factors for the mass movements are the vertical slopes and geological setting (Scheuer 1979), while the direct triggering factors are prolonged periods of extreme rainfall (Juhász 1999) as well as groundwater and river level fluctuations (Bányai et al. 2014). Due to their extremely high clay content and general geomorphologic properties, the high bluffs are extremely prone to landslides. Temporary landslides and mass movements have been reported over the entire section of the high bluff series during the past decade (Újvári et al. 2009; Balogh and Schweitzer 2011; Bányai et al. 2014; Kovács et al. 2015). However, only the landslides of the villages of Rácalmás and Dunaszekcső (Fig. 1) are known to be permanently active. Despite the significant economic losses caused by mass movements, few local monitoring networks have been established here (Újvári et al. 2009; Bugya et al. 2011; Bányai et al. 2014). Although the first PS tests by Del Ventisette et al. (2013) were successful at Rácalmás, spaceborne monitoring of other high bluffs has not yet been attempted.

Our first test site is in the village of Dunaszekcső (Dunaszekcső Test Site = TSD), situated in the central part of the southernmost section of the Hungarian high bluff series. The bluffs are found at an elevation of 120 m above sea level, 15 to 25 m above their surroundings (Moyzes and Scheuer 1978). A 4 km long series of rolling hills originating from fossil landslide masses is found between the bluffs and the Danube at an elevation of 100 to 110 m (Fig. 2). This is the only member of the Hungarian high bluff series where landslides are developed exclusively in Pleistocene deposits (Pécsi and Schweitzer 1995). The first landslide in Dunaszekcső occurred in 1862, and further movements were observed in 1965, 1976 and 2008 (Kraft 2011). A large data set of the recent monitoring campaigns is available from the most active zone of the high bluffs (Castle Hill), although data are scarce around the Castle Hill.

The second test site, in the village of Rácalmás (Rácalmás Test Site = TSR), is situated on the northern section of the Kulcs-Dunaújváros high bluff (Fodor et al. 1983). Here, the high bluffs reach a total length of 4570 m and rise 50 to 60 m above the mean water level

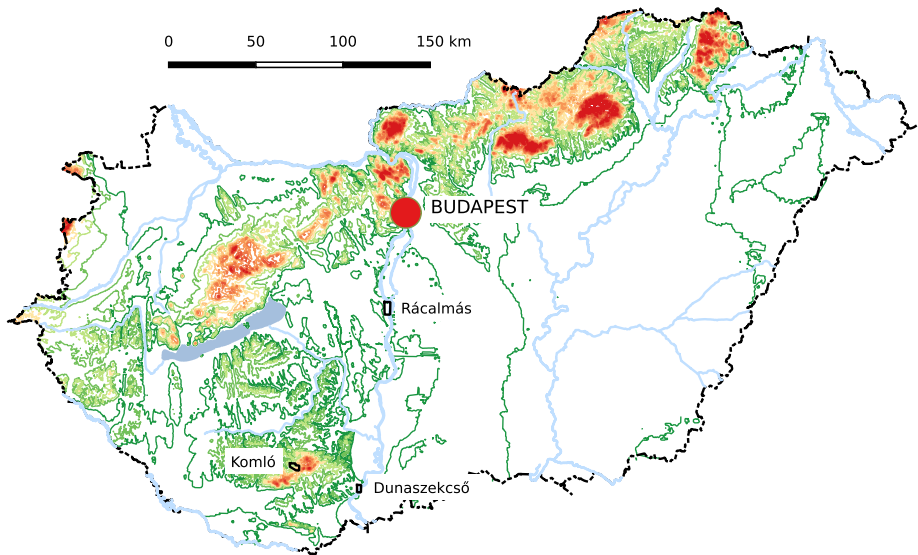


**Fig. 1** Location of the test and control sites

(90 m a.s.l.) of the Danube. This height is similar to that at Dunaszekcső (Balogh and Schweitzer 2011). A 200 to 300 m wide series of tongues of former landslides separate the high bluffs from an anastomosing side-branch of the Danube River here (Fig. 3). Recent landslides usually occurred on the Pleistocene and Miocene sediments of the former landslide masses. Landslide-generated economic losses have frequently been reported from here as part of Rácalmás is located on former landslide blocks (Fodor et al. 1983). The direction of displacements was perpendicular to the high bluffs, and the displaced blocks point toward the Danube. At the end of the 2000s, several retaining walls were built in the old village of Rácalmás (called Ófalu). Prevention costs reached more than 4 million €.

The town of Komló and its surroundings were chosen as a control site (Komló Control Site=CSK). The town lies 40 km west of Dunaszekcső and 100 km southwest from Rácalmás. The test site is located on the rolling hills of the Baranyai-Hegyhát microregion (Fig. 4), north of the Central Mecsek Hills. The microregion is built up of Mesozoic calcareous and carbonaceous rocks and locally amphibole-andesite volcanics (Némedi Varga 1967; Klespitz 2012), overlain by Tertiary and Quaternary sand and clay deposits (Lovász and Wein 1974). Interflues and hill tops reach an elevation of 300–350 m a.s.l. here, and valleys' bottoms lie at an elevation of 200–210 m a.s.l. Landslides are common on the steep slopes of the rolling hills and also across the town. Mass movements typically occur on clay-rich layers and steep slopes, while heavy rainfalls and anthropogenic activity may also contribute to the (re-)activation of mass movements (Lovász and Nagyvárad 1997). Rotational landslides and soil creep triggered by undermining, mining subsidence and natural processes were common phenomena here in the twentieth century (Szirtes 1994). The last coal mines were closed in 2000 (Kolozsvári and Pallós 2003; Nyers 2003), and only the andesite quarry in the southwestern part of the area has been in operation until today. Due to the lack of adequate monitored data, we should not exclude the appearance of mass movements, such as landslides, generated by the active subsidence of the ground

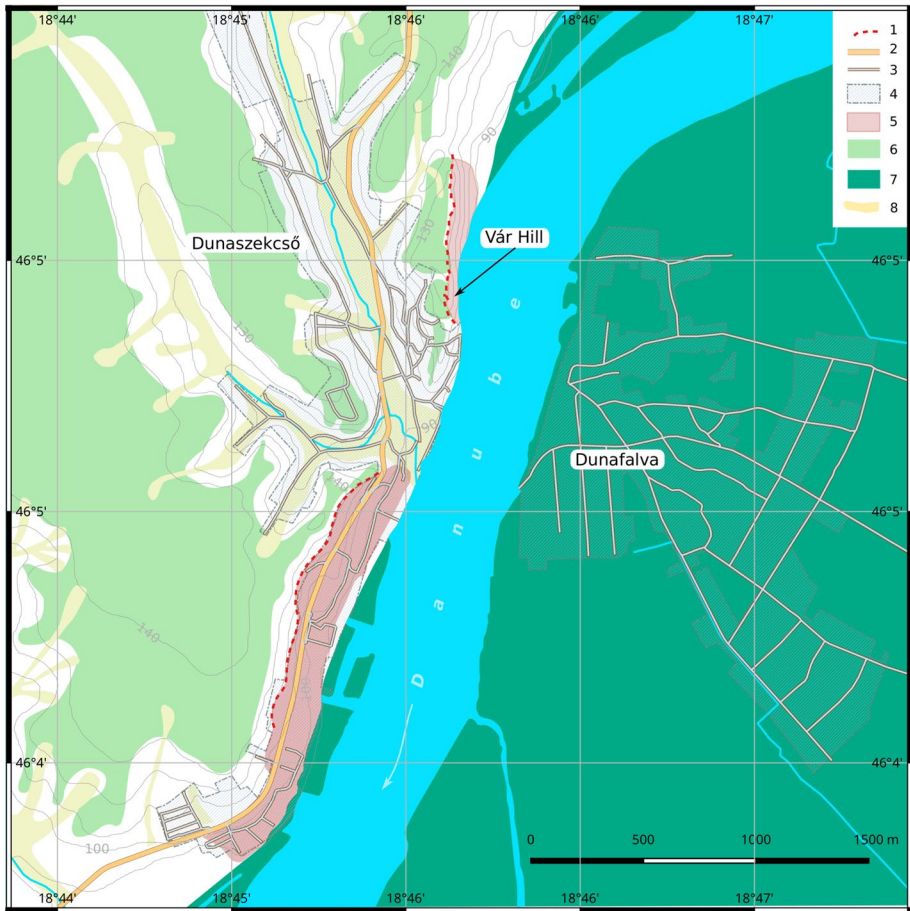


**Fig. 2** The geomorphologic map of the village of Dunaszekcső (TSD); 1=main escarpment, 2=primary road, 3=secondary, tertiary and residential roads, 4=residential area, 5=slopes affected by recent landslides, 6=loess plateau, 7=floodplain, island, 8=valley

surface. In addition, we may suppose that mine dumps, tailings and slopes of the andesite quarry are the morphologically most active surfaces of the area. Landslide-affected slopes are commonly observed in TSD, TSR and CSK under various land cover types. Densely vegetated low-coherence terrains are common here. In urban areas, however, coherence is high and numerous scatterers are detectable.

## 2 Materials and methods

### 2.1 Materials

Sentinel-1A Interferometric Wide Swath (IW) single look complexes (SLC) were downloaded from the ESA’s Sentinels Scientific Data Hub (<https://scihub.copernicus.eu>). They have been

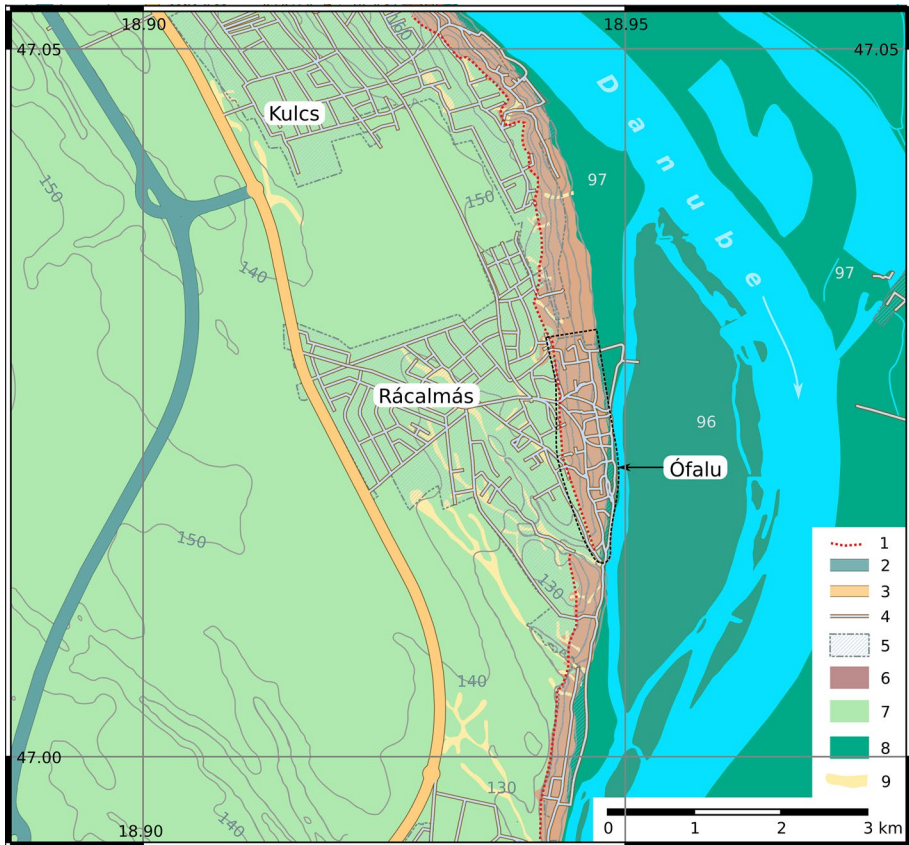


**Fig. 3** The geomorphologic map of the villages of Kulcs and Rácalmás (TSR); 1=main escarpment, 2=highway, 3=primary road, 4=secondary-, tertiary- and residential roads, 5=residential area, 6=slopes with recent landslides, 7=loess plateau, 8=floodplain, island, 9=valley

acquired in Terrain Observation with Progressive Scan SAR (TOPSAR) mode, which differs from the widely used Stripmap mode. Here, every single SLC is built up from several bursts (ESA 2013). Bursts are overlapped with their neighboring pairs and suitable for InSAR applications. However, especially when a region of interest (ROI) intersects bursts and covers only a fragment of one or more bursts, user should carefully prepare the sample selection and coregistration processes. On the other hand, with the selection of a single burst (considering a smaller ROI), they significantly reduce both storage needs and computational time, thus making InSAR processing manageable. Sentinel-1 SLCs cover almost one and a half year (Table 1) in ascending and descending geometry for the selected test areas. The maximum unambiguous displacement rate is one quarter of the wavelength, between the closest acquisitions. Despite the longer image separation periods, these image acquisition intervals still offer a unique opportunity to analyze landslides slower than 1.4 cm/14–16 days.



**Fig. 4** The geomorphologic map of the town of Komló (CSK); 1 = valley, 2 = ridges 3 = slopes, 4 = closed coal mine, 5 = andesite quarry, 6 = mine dumps, 7 = residential areas, 8 = railway, 9 = road

**Table 1** Temporal distribution of the analyzed images at the test areas in days

	TSD		TSR		CSK	
	Ascending	Descending	Ascending	Descending	Ascending	Descending
Min	12	12	12	12	12	12
Max	36	48	36	48	36	48
SD	5	8	5	7	5	8
Average	14	16	14	16	13	16
Mode	12	12	12	12	12	12
Num	39	34	42	37	43	36

*min* minimum lag between images, *max* maximum, *SD* standard deviation and *num* number of images

## 2.2 Methods

### 2.2.1 Geomorphologic mapping

Firstly, we collected field evidence and indicators of surface displacement from the three test sites. Field work and photodocumentation were done in March of 2016. As the test sites have been investigated in detail over the last decades by numerous authors, maps and published displacement data have also been used to identify possible displacement zones.

The general geomorphologic properties of the test sites, published data (Bugya et al. 2011; Del Ventisette et al. 2013; Kovács et al. 2015) and maps (Scheuer 1979; Fodor et al. 1983; Lovász and Nagyvárad 1997) were checked by field observations and represented on geomorphologic maps (Figs. 2, 3, 4). The sketches are based on the contour lines of 1:10,000-scale topographic maps.

## 2.2.2 PSI processing method

PSI processing of ascending and descending Sentinel-1A SLCs has been done using the SARscape 5.2.1. module of Envi 5.3.1. The implemented PSI algorithm is based on the original PS method (Ferretti et al. 2001). However, the SARscape method does not exclusively focus on PSI candidates, selected from their amplitude stability, but on all the pixels, selected due to their phase stability (PSI temporal coherence). As a theoretical background, we note that phase values, received by a SAR antenna and used for displacement extraction, depend on the following factors (Hein 2004):

$$\Delta\varphi_i(x, y) = \Delta\varphi_{\text{disp}} + \Delta\varphi_{\text{topo}} + \Delta\varphi_{\text{atm}} + \varphi_{\text{res}},$$

where  $\Delta\varphi$ ,  $\Delta\varphi_{\text{disp}}$ ,  $\Delta\varphi_{\text{topo}}$ ,  $\Delta\varphi_{\text{atm}}$  and  $\varphi_{\text{res}}$  are phase, displacement, topographic error, atmospheric artifacts and thermal noise, respectively. Topographic errors and atmospheric artifacts strongly limit displacement recognition, especially during conventional InSAR processing. Thus, PSI, such as other multi-interferogram techniques, operates with a set of SAR images to extract the above components and reduce their effect on the final results.

Although the test sites are of limited extent (a few km<sup>2</sup>), a region of interest (ROI) of about 10 × 15 km was selected from each image. This extended size of ROIs was needed for the successful coregistration and further processing steps, since the second step of PS algorithm (First inversion) runs over subregions of 5 × 5 km. All images (slaves) were coregistered onto a selected master image (Fig. 5), during the coregistration step. Over-sampling factor 4 was used to avoid the effect of fast fringes. Following the coregistration, interferograms were generated for each slave and the master image. For the interferogram flattening, SRTM-v4 DEM was used. It should be pointed out that the quality of the DEM has an effect on the success of the topography removal from the differential interferograms; hence, it affects the final result. During the next step (first inversion), residual height and displacement velocity were modeled and exploited to interferogram re-flattening. PSI method focuses on point like, stable scatterers (persistent scatterers), with well-characterized geometry (Pasquali et al. 2014). The investigated area was divided into subareas of 25 km<sup>2</sup>. The amplitude stability was used for selecting a reference point for each subarea. Further processing steps were performed on all pixels, related to the reference pixel. Later, they were merged, hence referred to a single reference pixel.

It is crucial that the algorithm is designed to estimate point displacements with a linear trend. Points with nonlinear displacements are not identified as a PS; hence, they are not present in the final result. APS was removed after the first estimation of the velocity and height correction (Ferretti 2014). Atmospheric artifacts have been removed using spatially low-pass and temporally high-pass filters, since APS is highly correlated in space, but poorly in time (Ferretti et al. 2001; Belmonte et al. 2017). It should be noted that low- and high-pass filter sizes were 365 days and 1200 m. For geocoding data, 0.75 coherence threshold and 20 m pixel size were used. As a final result, line of sight (LOS) velocities of the scatterers were calculated. LOS velocity describes the velocity of scatterers compared to the satellite position in each geometry. 2D (vertical and horizontal) displacements



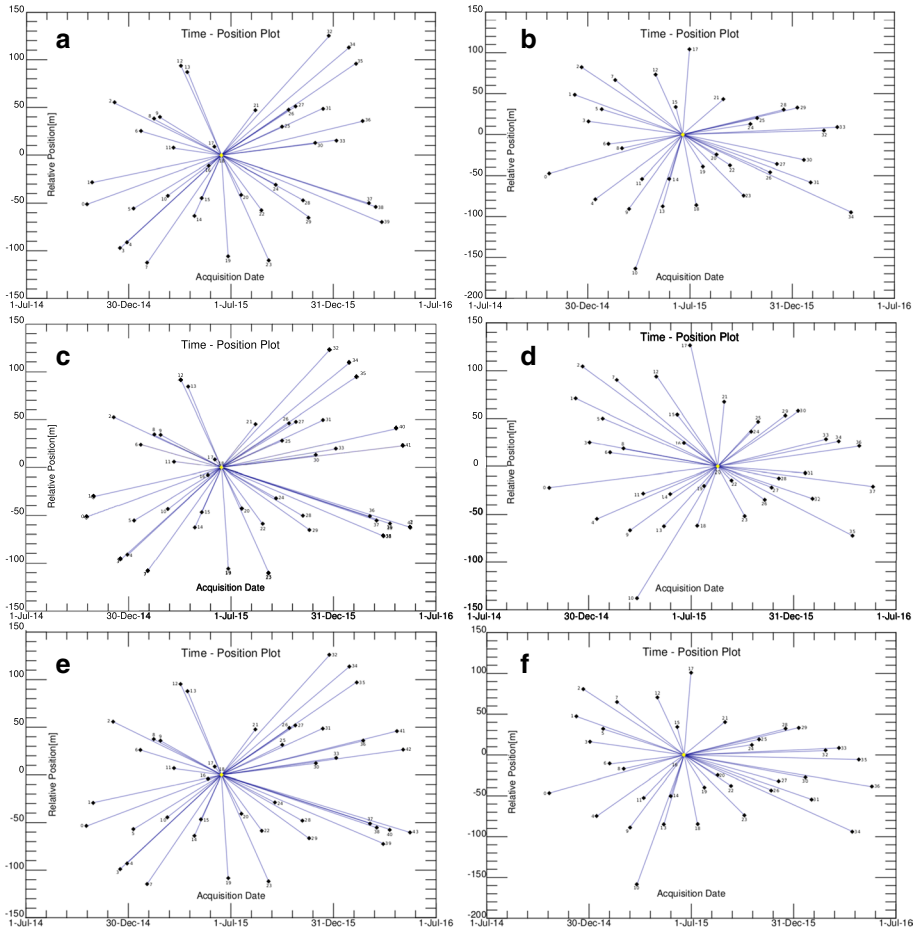


**Fig. 5** Time position graphs (connection graphs) of Sentinel-1A TOPSAR images during PS stacking processes. **a** TSD ascending geometry, **b** TSD descending geometry, **c** TSR ascending geometry, **d** TSR descending geometry, **e** CSK ascending geometry and **f** CSK descending geometry

of scatterers are interpretable combining LOS velocities of ascending and descending geometries.

### 2.2.3 Data analysis

Results from the PSI processes were imported into GRASS GIS 7.2.0 for further analysis. As a first step, formerly used ROIs were cut to the displacement zones and their proximal ‘stable’ surroundings to reduce the number of data and processing time.

Several indices describe the quality of PSI the measurements. Among them velocity precision ( $V_p$ ) and height precision ( $H_p$ ) have a direct link to the phase changes, but  $H_p$  is estimated from the phase component which is linearly proportional to the normal baseline. Therefore, during data processing, we focused on the LOS velocity and  $V_p$  of PSI points.  $V_p$  is the standard deviation of the displacement error,  $\Delta R$  (Just and Bamler 1994),

$$V_p = \sigma_{\Delta R} = \frac{\lambda}{4\pi} \cdot \sqrt{\frac{1 - \gamma^2}{2\gamma^2}}, \quad (1)$$

where  $\lambda$  = wavelength,  $\gamma$  = interferometric coherence of the current pixel of interest. Equation 1 describes the functional relation between the phase and the displacement, so it was considered the main tool for quality control. To obtain measurement quality of the individual PSI points, relative precision ( $r$ ) was calculated:  $r = (V_p / \text{LOS velocity}) \cdot 100$ . If the  $|r|$  of an individual PSI point is higher than 100, then the precision value is larger than the measured velocity, and therefore, real velocity can be either negative or positive. To avoid these low-quality measurements, points with low relative precision ( $|r| > 100$ ) were ignored.

Remaining points of each geometry were displayed on separate maps to observe the spatial pattern of points. The objective of the step-by-step displaying and testing of data was to identify a velocity threshold, where noise-like patterns disappear and displacement zones emerge. Each map contained points with velocities lower than 0 mm/year (circles with blue color) and higher than 0 mm/year (circles with red color). Velocity was increased and decreased step by step, using a 1 mm iteration procedure, to values ranging between +10 and –10 mm/year on separate maps. If part of the test site contained points with negative and positive velocity values close to each other and the distribution of points could not be explained by any geomorphologic or other well-known physical reason, the measured values were considered noise.

### 3 Results

As a first result, high density of scatterers was equally observed at test and control sites. The distribution of scatterers clearly corresponded to the location of the built-up areas in the case of both test sites. Only the Castle Hill landslide at TSD was an outlier here, due to its dense vegetation cover. Several points were also identified on the bare surfaces of the andesite quarry and extensive mine dumps at the southeastern tip of CSK. Point spatial densities of the investigated areas fluctuated between 396 and 620 points/km<sup>2</sup>. When points with  $|r| < 100$  were exclusively considered, then approximately half of the scatterers were discarded and point spatial densities decreased to 178–360 points/km<sup>2</sup>. With the step-by-step analysis of the scatterer velocities, point density further decreased (Fig. 6). High scatterer density of the ascending geometry was found for TSD and TSR; however, for CSK, the descending geometry was characterized by a higher spatial density of scatterers.

Scatterers with positive and negative LOS velocities are commonly found next to each other in TSD (Fig. 7A, E) when velocity thresholds of 0 to 5 mm/year were applied

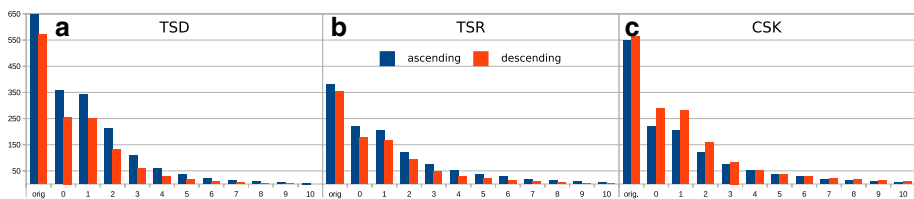


**Fig. 6** Spatial density of scatterers at the test sites according to the velocity iteration steps. **a** TSD; **b** TSR; **c** CSK. (y axis = point density [points/km<sup>2</sup>]; x axis = velocity iterations [mm], where  $|r| < 100$ ; orig. = original PSI density, ascending = ascending geometry, descending = descending geometry)

(Fig. 7B, F). It reflects a general, strong noise pattern of PSI data. By increasing the velocity threshold, a clearly visible group of points with negative LOS velocity appear in the southern part of TSD in *ascending geometry* (b in Fig. 7B–D). Moreover, points with negative and positive velocities also appear in the same area in *descending geometry* (b in Fig. 7F–H); however, they are distinct in space. Although the mentioned points show a clear spatial distribution, the remaining areas reflect a strong noise pattern. This noise pattern disappears when point velocities are higher than +6 or lower than –6 mm/year (Fig. 7C, G). At a velocity threshold of 7 mm/year, only a few points with positive velocities remain in ascending geometry (Fig. 7D) and only a few with negative velocities continue to exist in descending geometry (Fig. 7H). Here, displacements in different directions are well separated from each other in both geometries. At the same threshold, overlaps were infrequently observed between the two different geometry points. Despite the low

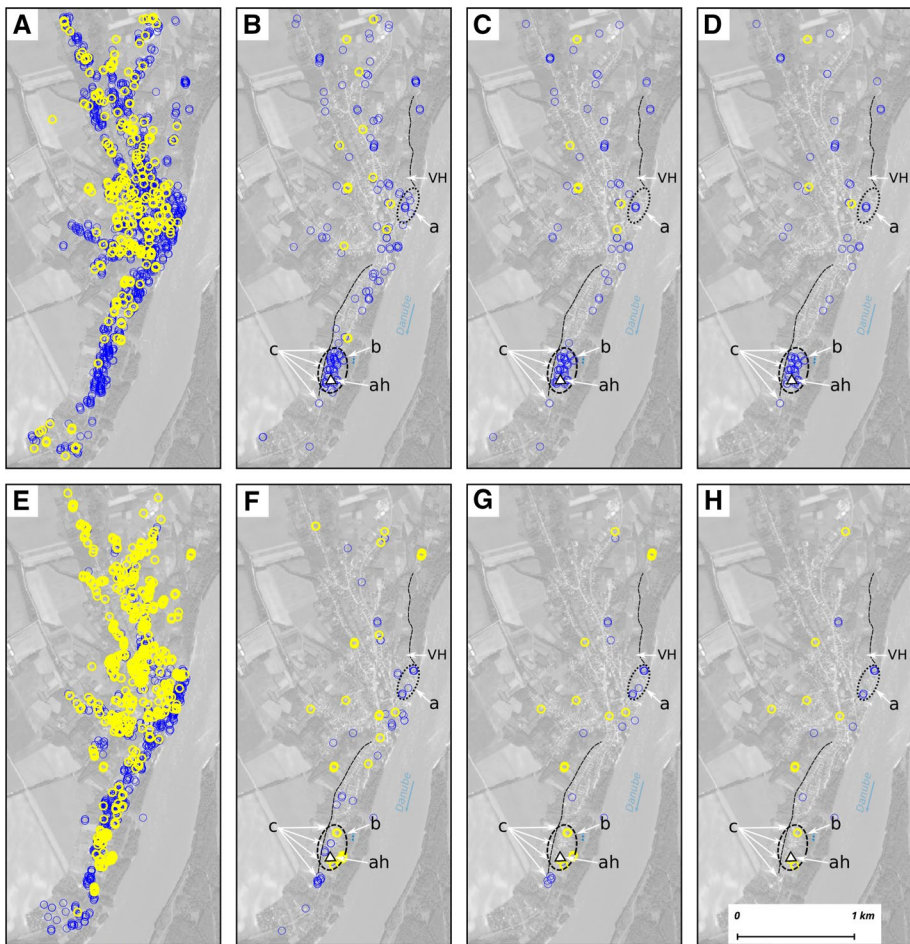


**Fig. 7** Scatterers at TSD, according to LOS velocity iteration steps. ( $|l| < 100$ , blue circle = negative LOS velocity, yellow circle = positive LOS velocity, **A–D** ascending geometry, **E–H** descending geometry, **A**  $0 > \text{velocity} > 0$ , **B**  $-5 > \text{velocity} > 5$ , **C**  $-6 > \text{velocity} > 6$ , **D**  $-7 > \text{velocity} > 7$ , **E**  $0 > \text{velocity} > 0$ , **F**  $-5 > \text{velocity} > 5$ , **G**  $-6 > \text{velocity} > 6$ , **H**  $-7 > \text{velocity} > 7$ , VH = Vár Hill, a = subsidence at VH, b = lateral movement on the southern part of TSD, c = subsidence front of the scarp, ah = location of abandoned house

number of scatterers and the increased velocity thresholds, displacements are visible in the southern part of the village (b in Fig. 7B, C, D, F, G, H) (moving away from the satellite in ascending geometry and moving toward the descending orbit satellite). Points with negative velocities were detected also south of the recently actively moving block of the Castle Hill landslide in both geometries (a in Fig. 7B, C, D, F, G, H); however, their overlap is ambiguous. In addition, individual scatterers are permanently present in the entire area in both geometries and also at higher velocity thresholds.

PSI results from TSR show a noise pattern similar to that of TSD. The only difference is the active block of the Ófalu landslide which is clearly visible even at low-velocity thresholds (Fig. 8). Scatterers show a uniform behavior (negative velocities in ascending and positive velocities in descending geometry) there. No noise was detected here, but noise was common at all locations of the Rácalmás test site (Fig. 8A, E). This strong noise pattern begins to disappear at a velocity threshold of 6 mm/year (Fig. 8C, G) and becomes completely absent at a velocity threshold of 7 mm/year (Fig. 8D, H). The only area where adjacent points are moving in the opposite direction is in the western part of the site in descending geometry and only spreads over a small area, with a few scatterers (rc in Fig. 8F–H). They are also present at more positive and more negative velocities, however, only in descending geometry.

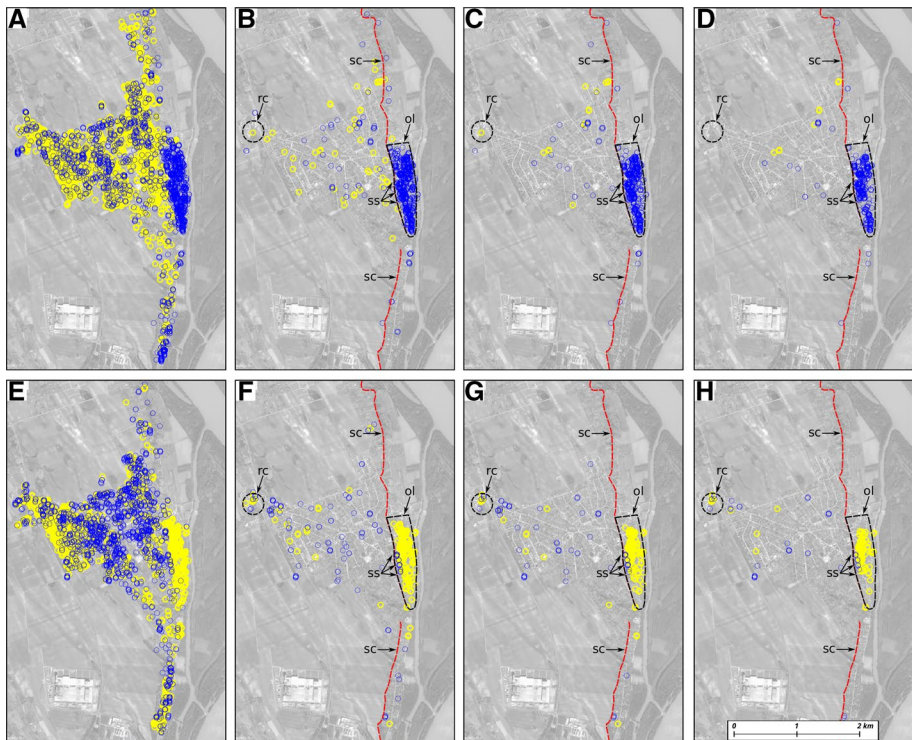


**Fig. 8** Scatterers at TSR, according to LOS velocity iteration steps. ( $|l| < 100$ , blue circle = negative LOS velocity, yellow circle = positive LOS velocity, **A–D** ascending geometry, **E–H** descending geometry, **A**  $0 > \text{velocity} > 0$ , **B**  $-5 > \text{velocity} > 5$ , **C**  $-6 > \text{velocity} > 6$ , **D**  $-7 > \text{velocity} > 7$ , **E**  $0 > \text{velocity} > 0$ , **F**  $-5 > \text{velocity} > 5$ , **G**  $-6 > \text{velocity} > 6$ , **H**  $-7 > \text{velocity} > 7$ , ol = Ófalu Landslide, sc = scarp, ss = subsidence front of the scarp, rc = road construction

At a threshold of 7 mm/year, there are spatially concentrated points on the landslide in Ófalu, showing that points are moving away from the satellite in ascending geometry (ol in Fig. 8D) and they are moving toward the satellite in descending geometry (ol in Fig. 8H). Moreover, in descending geometry, on the western margin of the landslide block a few points are moving away from the satellite. These points are aligned into a curved line (ss in Fig. 8H). At an increased velocity threshold, like at TSD, individual points are present, but their spatial distribution indicates a rather random pattern.

Points with negative LOS velocity dominate the western part of CSK, as long as scatterers are moving toward the satellite on the eastern side in both geometries at a 0–5 mm/year velocity threshold (Fig. 9B, F). The mentioned noise pattern is also common here, in the entire site up to a velocity threshold of 6 mm/year (Fig. 9C, G); however, they are less common in the eastern part of the area, especially at the elongated mine dump (md in Fig. 9C, G) and the northwestern foreground of the dump in the valley floor of the Kaszárnya Creek (kc in Fig. 9C, G). This diverse and spatially uncorrelated pattern starts to disappear at a velocity threshold of 6 mm/year and is almost absent at a velocity threshold of 7 mm/year (Fig. 9D, H). At and above this threshold, the western part of the area is sparsely populated by scatterers moving in the opposite direction. They are not neighboring points and represent rather individual displacements. Furthermore, scatterers of the northern and northeastern parts of the southern mine dumps (md in Fig. 9D, H) represent areas that have been displaced toward the satellite in both acquisitions. In accordance with the aforementioned Kaszárnya Creek site (ck in Fig. 9D, H), the spatial coverage of the scatterers also overlaps at this site. In the andesite quarry (aq in Fig. 9D, H), several scatterers were found on both the satellite-facing slopes and the opposite directions. In the first case (satellite-facing slopes) scatterer velocities are positive values, while for the opposite slopes they bear negative values.

Considering former C-band sensors, such a noise, observed by Sentinel-1 imagery and produced by PSI interferometry, is unusual. Nevertheless, it is present under the field conditions described above. Noise may be introduced into the final results by multiple factors during the interferometric stacking process. During the interferometric procedure, an important step is the removal of topographic phase component. To model topography, SRTM-v4 DEM is widely used. However, the resolution of the DEM is low compared to the 20 m ground resolution of Sentinel-1. Moreover, SRTM was introduced more than 10 years ago. A conventional technique for the improvement of the DEM is the use of interferometric measures themselves for obtaining a more precise DEM. Exploiting interferometric DEM is also applicable for the successful removal of topographic errors. However, Sentinel-1 was introduced with a short baseline (Bn) and orbital tube concept. The shorter the Bn, the less accurate the estimation of the topography is, thus, for Sentinel-1 sensing capability of the topography is less effective than of older sensors. Consequently, Sentinel-1A images are less suitable for DEM generation.

A second factor affecting measurement quality is vegetation cover and hence the low coherence of the area. This factor may introduce errors during the interferometric step and phase unwrapping. Nevertheless, improved temporal separation of Sentinel-1A plays is instrumental for the preservation of coherence and scatterers. Increasing the coherence threshold would be the base of noise reduction for short time series. Using a larger coherence value could help the separation of scatterers with higher phase stability. However, it would reduce scatterer density to the value obtained by Del Ventisette et al. (2013) using an Envisat data set. PSs with high coherence threshold could be more reliable for successful calculations and may prevent the loss of low-velocity scatterers.

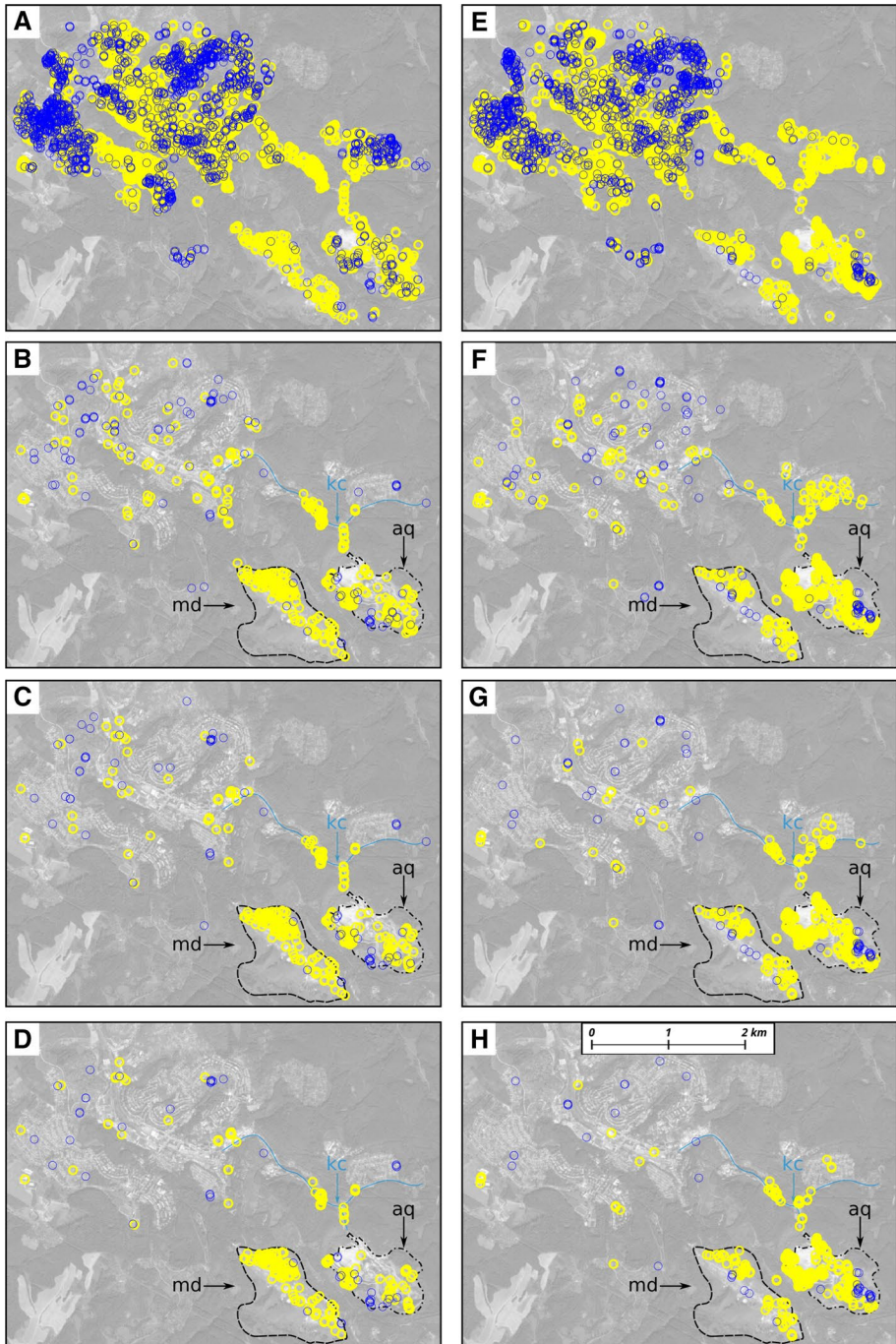


**Fig. 9** Scatterers at CSK, according to LOS velocity iteration steps. ( $|v| < 100$ , blue circle=negative LOS velocity, red cross=positive LOS velocity, **A–D** ascending geometry, **E–H** descending geometry, **A**  $0 > \text{velocity} > 0$ , **B**  $-5 > \text{velocity} > 5$ , **C**  $-6 > \text{velocity} > 6$ , **D**  $-7 > \text{velocity} > 7$ , **E**  $0 > \text{velocity} > 0$ , **F**  $-5 > \text{velocity} > 5$ , **G**  $-6 > \text{velocity} > 6$ , **H**  $-7 > \text{velocity} > 7$ , kc=Kaszárnya Creek, md=mine dump, aq=andesite quarry

Another important factor is the incidence angle of sensing in Interferometric Wide Swath (IW) mode which ranges between  $31^\circ$  and  $46^\circ$  (ESA 2013). This angle is about twice the corresponding value of the former C-band sensors; therefore, their signals penetrate the ionosphere and the troposphere through a longer path during the sensing and receiving processes. This introduces a third noise component (APS) into the measurements. As we formerly noted, APS filtering is difficult on short time series. APS has a stochastic nature, which means that it is highly correlated in space, but poorly in time (Ferretti et al. 2001; Belmonte et al. 2017). To remove spatial component of APS, a low-pass filter was used for both the control and the test sites. The smaller the filter size, the stronger the effect of filtering. However, the filter can also remove spatially correlated real displacements if the filter size is equal to or smaller than the spatial extent of the displacement zones. The filter size was 1200 m for all three test sites, which is slightly wider than the investigated landslide areas; therefore, it is impossible to further enhance low-pass filter performance here. For temporal APS filtering, a high-pass filter was used. With a larger window size, an increased temporal filter performance is obtained. The most severe limitation here is the short length of the data sets, which hinders filter enhancement. Thus, due to the unsuccessful use of the high-pass filter, APS strongly affects measured displacement. For a successful APS filtering, significantly longer time series are needed, even if the studied displacements span a short period of time.

## 4 Discussion

Mean spatial scatterer density, obtained in the current study, is approximately 8–10 times higher in all three test sites than the 48–52 points/km<sup>2</sup> values calculated formerly by Del Ventisette et al. (2013) at TDR, using ERS and Envisat data. However, using the relevant scatterers, where  $|\rho| < 100$ , point density decreased by 50% and it was further heavily reduced at a velocity threshold of 6–7 mm/year. Nevertheless, point spatial densities of the area depend on land cover and only contain valuable information when compared with the results of different measurements within the same ROI. This comparison is questionable, like in the currently described case, where we were unable to accurately reconstruct the ROI obtained by Del Ventisette et al. (2013). Firstly, increased point spatial densities calculated from Sentinel-1A can be interpreted as a result of improved sensor and acquisition mode (TOPSAR). Secondly, the presence of scatterers highly depends on their temporal stability (temporal coherence). Clearly, scatterers are more detectable with the 14 to 16-day temporal acquisition intervals over a period of about a year and a half, than acquisitions over a 10-year sensing period with a temporal separation of about 35 days.

Differences in the number of scatterers in ascending and descending geometries are the consequence of the position and aspect of the slope (topography) of the individual test and control sites (Ferretti 2014). Scatterers in layover or in foreshortening are well represented in the other geometry. Therefore, using both geometries, more detailed displacement information is obtained.

Despite the noise, displacement zones are clearly visible for each site and their remotely sensed spatial extent well corresponds to the field-observed displacement zones. However, exact spatial separation of the displacement zones from the stable background is challenging if all the final results of the PSI processing are considered. Removing points with  $|\rho| > 100$  is the first step of data filtering. It reduces the number of points approximately to the half of the original at all sites. Accordingly, about 50% of all points of the first results

have no geomorphic meaning and value for further consideration. Moreover, scatterers, without the above-mentioned noise, are only detectable below the velocity thresholds of  $-6$  to  $7$  and over  $+6$  to  $+7$  mm/year at TSD, TSR and CSK. In addition to the observed typical field velocity thresholds, values were also obtained experimentally using geomorphologic maps for visual interpretation. Presumably, some noise-affected scatterers reflect real field conditions and contain valuable information. However, they were removed during the iteration steps.

The location of the main displacement zone is clear in the southern part of TSD, but just in ascending geometry and above the velocity threshold of  $6-7$  mm/year (b in Fig. 7C, D, G, H). Maximum LOS velocities of the detection points reached 14 mm/year, which corresponds to the extremely slow category and class 1 by the classification scheme published by Cruden and Varnes (1996). According to the classification of Cruden and Varnes (1996), the state of activity of the slide is reactivated and moving. This group of scatterers, moving away from the satellite, points out remarkable subsidence and slow lateral movements of the landslide mass in front of the high bluffs. However, in descending geometry only a few scatterers are present here and the two geometries do not overlap completely; therefore, the identification of the exact type and extent of mass movement is challenging. Field information and dilatation cracks on abandoned houses (Fig. 10) suggest strong lateral shear stress here, which is generated by mass subsidence and mainly lateral movements from the high bluff toward the Danube. In accordance with the displacements, scatterers prove a clear subsidence at the bluff base caused by the lateral movement of the eastern part of the landslide. Other sporadic scatterers of the village reflect rather individual displacements of buildings. The only exceptions are in the northeast, at the base of the Castle Hill landslide (a in Fig. 7C, D, G, H), where velocities well reflect field conditions and subsidence rates.



**Fig. 10** Abandoned house on the active landslide mass at Dunaszekcső in October 2016 (location in Fig. 7)



Scatterers of TSR show a wider displacement area, concentrated on the Ófalu landslide. Scatterer data suggest that the lateral movement of the entire Ófalu area is manifested in sliding toward the Danube (at TSD). Nonetheless, we should point out that subsidence occurs at the *base* (ss in Fig. 8C, D, G, H) and follows the alignment of the bluff. Observations of the consequences of the extremely slow movement (up to 15 mm/year) of the landslide (according to Cruden and Varnes 1996) and the detection of damage to buildings is uncertain since residents permanently move their belongings out of the damaged buildings. Unfortunately, following the thresholding, only a few scatterers remain north and south from the landslide; therefore, their number is insufficient for the precise delineation of the zones of displacement. However, slow-moving landslides should be present both in TSD and TSR, due to their similar geologic and geomorphologic build-up. Sporadic appearance of scatterers can be interpreted as smaller individual displacements, but field data are unavailable at this spatial resolution. Only one subsidence on the northwestern part of TSR (rc in Fig. 8C, D, G, H) can be associated with road construction.

Scatterers of CSK show a distinct uplift in the southeastern part of CSK and in the valley bottom of the Kaszárnya Creek, where both geometries are overlapped. Typical displacement velocities at this site reach 10 mm/year. These mass movements rather indicate expansion of the material of the mine dump due to uptake of water, i.e., is not considered a landslide. Higher velocities were observed in the andesite quarry (up to 23 mm/year): these movements are triggered by the creeping of the unconsolidated material. Nonetheless, interferometry is a relative measure and results (the velocity of scatterers) are always compared to ground control points (GCP). In the current case, GCP points are probably affected by the tectonic uplift of the Mecsek Mountains, where velocity values are comparable to the measured local displacements at the control site. To separate local displacements in the field [e.g., movements along mine dumps (md in Fig. 9C, D, G, H), the creep of the unconsolidated material in the andesite quarry (aq in Fig. 9C, D, G, H)], high-precision DGPS measurements of the control points are needed. This is not the case for TSD and TSR, since GCPs were placed in the stable background area at a great distance from the moving landslides where tectonic activity is low. Subsidence or uplift rates of less than 1 mm/year were measured there (Joó 1992). These values, however, are far below the accuracy of Sentinel-1 (considering the analyzed set of images). Nevertheless, for absolute displacement DGPS measurements are indispensable.

## 5 Conclusions

The ambiguous behavior of scatterers at low-velocity values can be interpreted as massive noise all over the TSD, TSR and CSK, which may have derived from various sources. Generally, InSAR measurements produce noise; however, further processing techniques aim the reduction of noise without the loss of significant data. Despite the careful processing of Sentinel-1A acquisitions, LOS displacement data remained noisy in TSD, TSR and CSK to threshold velocities of 6 to 7 mm/year. Hence, scatterers, moving slower than the above-mentioned threshold, were corrupted by noise and are devoid of geomorphologic meaning for the observer. However, points above the threshold carry valuable and useful information on surface deformation processes. Displacement zones of the analyzed sites are well visible without filtering (thresholding) the noise, but their accurate mapping and clustering are highly hampered. We consider APS and the shortage of sufficiently long time series as the main reasons of noise in our data. Therefore, to increase measurement

accuracy, additional improvements and verification protocols are needed. The use of high-quality DEMs and mainly the increasing length of time series, i.e., time range between the first and last images, will likely further reduce data loss and optimize the signal-to-noise ratio during the interferometric processing steps. To overcome noise-triggering challenges of short time series, increased coherence could provide more reliable PSs. Finally, all readers should consider the above signal-to-noise ratio relevant and adequate for research sites with similar coherence where temporal spacing and duration of images are comparable.

**Acknowledgements** The authors are grateful to Dr. Noémi Sarkadi for her valuable comments and suggestions. The current research was funded by the GINOP-2.3.2.-15-2016-00055 project. The present scientific contribution is dedicated to the 650th anniversary of the foundation of the University of Pécs, Hungary. The project has been supported by the European Union, co-financed by the European Social Fund Grant No.: EFOP-3.6.1.-16-2016-00004 entitled by Comprehensive Development for Implementing Smart Specialization Strategies at the University of Pécs.

**Open Access** This article is distributed under the terms of the Creative Commons Attribution 4.0 International License (<http://creativecommons.org/licenses/by/4.0/>), which permits unrestricted use, distribution, and reproduction in any medium, provided you give appropriate credit to the original author(s) and the source, provide a link to the Creative Commons license, and indicate if changes were made.

## References

- Balogh J, Schweitzer F (2011) Felszínmozgásos folyamatok a Duna Gönyű-Mohács közötti magasparti szakaszain. [Mass movements along the Danubian high bluff between Gönyű and Mohács] In: Schweitzer F (ed) *Katasztrófák tanulságai. Stratégiai jellegű természetföldrajzi kutatások* [Conclusions of catastrophes. Physical geographical research for strategic purposes]. Elmélet-Módszer-Gyakorlat, MTA FKI, Budapest pp 101–142
- Bányai L, Mentés G, Újvári G, Kovács M, Czap Z, Gribovszki K, Papp G (2014) Recurrent landsliding of a high bank at Dunaszekcső, Hungary: geodetic deformation monitoring and finite element modeling. *J Geodyn* 47:130–141
- Barra A, Monserrat O, Mazzanti P, Esposito C, Crosetto M, Mugnozza GS (2016) First insights on the potential of Sentinel-1 for landslides detection. *Geomat Nat Hazards Risk* 7:1874–1883. <https://doi.org/10.1080/19475705.2016.1171258>
- Béjar-Pizarro M, Notti D, Mateos RM, Ezquerro P, Centolanza G, Herrera G, Bru G, Sanabria M, Solari L, Duro J, Fernández J (2017) Mapping vulnerable urban areas affected by slow-moving landslides using Sentinel-1 InSAR Data. *Remote Sens* 9:876–893. <https://doi.org/10.3390/rs9090876>
- Belmonte A, Refice A, Bovenga F, Pasquariello G, Nutricato R (2017) Unwrapping-free interpolation of sparse DInSAR phase data: experimental validation. *Int J Remote Sens* 38:1006–1022
- Bugya T, Fábrián SÁ, Görös NL, Kovács IP, Radvánszky B (2011) Surface changes on a landslide affected high bluff in Dunaszekcső (Hungary). *Central Eur J Geosci* 3:119–128
- Casagli N, Cigna F, Bianchini S, Hölbling D, Füreder P, Righini G, Del Conte S, Friedl B, Schneiderbauer S, Iasio C, Vlčko J, Greif V, Prose H, Granica K, Falco S, Lozzi S, Mora O, Arnaud A, Novali F, Bianchi M (2016) Landslide mapping and monitoring by using radar and optical remote sensing: examples from the EC-FP7 project SAFER. *Remote Sens Appl Soc Environ* 4:92–108. <https://doi.org/10.1016/j.rsase.2016.07.001>
- Chen Q, Cheng H, Yang Y, Liu G, Liu L (2014) Quantification of mass wasting volume associated with the giant landslide Daguangbao induced by the 2008 Wenchuan earthquake from persistent scatterer InSAR. *Remote Sens Environ* 152:125–135
- Chung CJF, Fabbri AG (2003) Validation of spatial prediction models for landslide hazard mapping. *Nat Hazards* 30:451–472
- Cruden DM, Varnes DJ (1996) Landslide types and processes. Transportation research board, U.S. Nat Acad Sci Spec Rep 247:36–75
- Del Ventisette C, Ciampalini A, Calò F, Manunta M, Paglia L, Reichenbach P, Colombo D, Mora O, Strozzi T, Garcia I, Mateos R, Herrera G, Füsi B, Graniczny M, Przylucka M, Retzo H, Moretti S, Casagli N, Guzzetti F (2013) Exploitation of large archives of ERS and ENVISAT C-Band SAR data to characterize ground deformation. *Remote Sens* 5:3896–3917

- ESA (2013) Sentinel-1 User Handbook. <https://www.scribd.com/doc/259520850/Sentinel-1-User-Handbook>. Accessed 28 Dec 2018
- Ferretti A (2014) Satellite InSAR data. Reservoir monitoring from space, EAGE Publications
- Ferretti A, Prati C, Rocca F (2001) Permanent scatterers in SAR interferometry. *IEEE Trans Geosci Remote Sens* 39:8–20
- Fodor T-né, Horváth Z, Scheuer G, Schweitzer F (1983) A rácalmási—kulcsi magaspártok mérnökgeológiai térképezése [Engineering geological mapping of Rácalmás and Kules high bluff]. *Földtani Közlöny [Bull Hung Geol Soc]* 113:313–332
- Glade T, Anderson M, Crozier MJ (2005) Landslide hazard and risk. Wiley, Chichester
- Hein A (2004) Processing of SAR data. Fundamentals, signal processing, interferometry. Springer, Berlin
- Herrera G, Notti D, García-Davalillo JC, Mora O, Cooksley G, Sánchez M, Arnaud A, Crossetto M (2010) Analysis with C- and X-band satellite SAR data of the Portalet landslide area. *Landslides* 8:195–206
- Herrera G, Gutiérrez F, García-Davalillo JC, Guerrero J, Notti D, Galve JP, Fernández-Merodo JA, Cooksley G (2013) Multi-sensor advanced DInSAR monitoring of very slow landslides: the Tena Valley case study (Central Spanish Pyrenees). *Remote Sens Environ* 128:31–43
- Jóó I (1992) Recent vertical surface movements in the Carpathian Basin. *Tectonophysics* 202:129–134
- Juhász Á (1999) A klimatikus hatások szerepe a magaspártok fejlődésében [Climatic influence on the development of high bluffs]. *Földtani Kutatás [Geol Res]* 3:14–20
- Just D, Bamler R (1994) Phase statistics of interferograms with applications to synthetic aperture radar. *Appl Opt* 33:4361–4368
- Klespitz J (2012) Bányaföldtani tapasztalatok a komlói andezitbányában [Mining geological experiences on the Komló andesite quarry]. *Építőanyag [Build Mater]* 64:18–21
- Kolozsvári S, Pallós P (2003) Az utolsó mecseki mélyművelésű szénbánya bezárása [Closure of the last under-cast coal mine in the Mecsek Mountains]. *Bányászati és kohászati lapok [J Min Metall]* 136:167–175
- Kovács IP, Fábrián SÁ, Radvánszky B, Varga G (2015) Dunaszekcső castle hill: landslides along the danubian loess bluff. In: Lóczy D (ed) *Landscapes and landforms of Hungary*. Springer, Cham, pp 113–120
- Kraft J (2011) Dunai magaspárt dunaszekcsői részletének rogyásos suvadásai [Landslides of the Danubian high bluff at Dunaszekcső]. In: Török Á, Vásárhelyi B (eds) *Mérnökgeológia—Közetmechanika [Engineering geology and rock mechanics]*. Hantken Kiadó, Budapest, pp 93–104
- Lovász G, Nagyvárad L (1997) Geomorphological impacts of urbanization: example of Komló, S-Transdanubia, Hungary. *Z Geomorphol Supplementband* 110:241–246
- Lovász G, Wein G (1974) A Délkelet-Dunántúl geológiája és felszínfejlődése [Geology and surface development of south eastern Transdanubia]. Manuscript. Baranya megyei Levéltár [Baranya County Archive], Pécs
- Moyzes A, Scheuer G (1978) A dunaszekcsői magaspártok mérnökgeológiai vizsgálata [Engineering geology of high bluffs at Dunaszekcső]. *Földtani Közlöny [Bull Hung Geol Soc]* 108:213–226
- Némédi Varga Z (1967) A Mecsek-hegységi andezitvulkánosság [Andesite volcanism of the Mecsek Mountains]. *Földtani Közlöny [Bull Hung Geol Soc]* 97:396–413
- Nyers J (2003) Zobák bánya bezárásához kapcsolódó vizsgálatok és megfigyelések [Experiences and researches on the closure of Zobák under-cast coal mine]. *Bányászati és kohászati lapok [J Min Metall]* 136:176–181
- Pasquali P, Cantone A, Riccardi P, Defilippi M, Ogushi F, Gagliano S, Tamura M (2014) Mapping of ground deformations with interferometric stacking techniques. In: Holecz F, Pasquali P, Milisavljevic N (eds) *Land applications of radar remote sensing*. InTechOpen, Rijeka. <https://doi.org/10.5772/58225>
- Pécsi M (1959) A magyarországi Dunavölgy kialakulása és felszínalaklata [Development and surface development of the Danube Valley]. *Földrajzi Monográfiák 3*. Akadémiai Kiadó, Budapest
- Pécsi M, Schweitzer F (1995) The lithostratigraphical, chronostratigraphical sequence of Hungarian loess profiles and their geomorphological position. *Loess inForm (Budapest)* 3:31–61
- Piacentini D, Devoto S, Mantovani M, Pasuto A, Prampolini M, Soldati M (2015) Landslide susceptibility modeling assisted by Persistent Scatterers Interferometry (PSI): an example from the northwestern coast of Malta. *Nat Hazards* 78:681–697
- Prats-Iraola P, Nannini M, Scheiber R, De Zan F, Wollstadt S, Minati F, Vecchioli F, Costantini M, Borgstrom S, De Martino, P (2015) Sentinel-1 assessment of the interferometric wide-swath mode. In: 2015 IEEE international geoscience and remote sensing symposium (IGARSS), pp 5247–5251
- Scheuer G (1979) A dunai magaspártok mérnökgeológiai vizsgálata [Geoengineering study of the high bluffs along the Danube]. *Földtani Közlöny [Bull Hung Geol Soc]* 109:230–254

- Singleton A, Li Z, Hoey T, Muller JP (2014) Evaluating sub-pixel offset techniques as an alternative to D-InSAR for monitoring episodic landslide movements in vegetated terrain. *Remote Sens Environ* 147:133–144
- Sowter A, Bin Che Amat M, Cigna F, Marsh S, Athab A, Alshammari L (2016) Mexico City land subsidence in 2014–2015 with Sentinel-1 IW TOPS: results using Intermittent SBAS (ISBAS) technique. *Int J Appl Earth Obs Geoinf* 52:230–242
- Szabó J (1996) Cszszamlásos folyamatok szerepe a magyarországi tájak geomorfológiai fejlődésében [Role of landslides on the surface development of Hungarian landscapes]. Kossuth Egyetemi Kiadó, Debrecen
- Szirtes B (1994) A mecseki kőszénbányászat [Coal mining in the Mecsek Mountains]. Kútforrás Kiadó, Pécs
- Tofani V, Raspini F, Catani F, Casagli N (2013) Persistent Scatterer Interferometry (PSI) technique for landslide characterization and monitoring. *Remote Sens* 5:1045–1065
- Tomás R, Li Z, Liu P, Singleton A, Hoey T, Cheng X (2014) Spatiotemporal characteristics of the Huangtupo landslide in the Three Gorges region (China) constrained by radar interferometry. *Geophys J Int* 197:213–232
- Újvári G, Mentés G, Bányai L, Kraft J, Gyimóthy A, Kovács J (2009) Evolution of a bank failure along the River Danube at Dunaszekcső, Hungary. *Geomorphology* 109:197–209
- Wasowski J, Bovenga F (2015) Remote sensing of landslide motion with emphasis on satellite multitemporal interferometry applications: an overview. In: Davies T (ed) *Landslide hazards, risk, and disasters*. Elsevier, Amsterdam, pp 345–403

**Publisher's Note** Springer Nature remains neutral with regard to jurisdictional claims in published maps and institutional affiliations.